

# Evidence for oxidation at the base of the nakhlite pile by reduction of sulfate salts at the time of lava emplacement

James W. Dottin III<sup>a,\*</sup>, Jabrane Labidi<sup>b</sup>, James Farquhar<sup>a</sup>, Philip Piccoli<sup>a</sup>,  
Ming-Chang Liu<sup>b</sup>, Kevin D. McKeegan<sup>b</sup>

<sup>a</sup> Department of Geology, University of Maryland, College Park, MD 20742, United States

<sup>b</sup> Department of Earth, Planetary, and Space Sciences, University of California, Los Angeles, CA 90095, United States

Received 6 March 2018; accepted in revised form 23 July 2018; available online 02 August 2018

## Abstract

The assimilation of sulfate by Martian melts could explain the highly oxidized state of some Martian nakhlite meteorites, such as those paired with MIL 03346 (MIL 090030, MIL 090032, and MIL 090136). Here, a combination of new sulfur isotope data, mineral composition and abundance data, and consideration of mineral textures is used to link assimilation of surface-derived Martian sulfate to oxidation of nakhlite melts. The magnitudes of the mass independent sulfur isotope signatures (negative  $\Delta^{33}\text{S}$ ) and the abundance of sulfide minerals accounts for much of the added oxygen implied by the occurrence of abundant skeletal titanomagnetite in the MIL pairs. Assimilation and reduction of sulfate amounts equivalent to that from 10's of centimeters of Martian sediment are required to account for an oxidation front extending ~1 m into the flow, a position previously proposed for MIL 03346, and implies a position at the bottom, rather than the top of a nakhlite flow. A similar positional and amount constraint is required for an alternative path for assimilation of sulfate from sulfate-rich brine. Assimilation and reduction of sulfate is therefore inferred to play a critical role in establishing both the enrichment in skeletal titanomagnetite within the lower portion of the nakhlite pile and the large  $\Delta^{33}\text{S}$  anomalies of the MIL pairs. Other nakhlites with smaller  $\Delta^{33}\text{S}$  anomalies and less titanomagnetite would occupy positions farther away from the source of sulfate.

© 2018 Elsevier Ltd. All rights reserved.

**Keywords:** Nakhlite; Sulfur isotopes; Assimilation; Oxidation; Mass independent; MIL 090030; MIL 090032; MIL 090136

## 1. INTRODUCTION

The nakhlite meteorites are clinopyroxene rich cumulates that are thought to originate on Mars in one or more thick volcanic flows of a minimum 15–20 meters thickness (e.g. [Lentz et al., 1999](#)). Cumulus and intercumulus phases are consistent with at least two stages of crystallization. Two hypotheses have been proposed to explain the cumulate minerals: cumulate phenocrysts formed either in a single event in a staging chamber ([Mikouchi et al., 2003](#); [Treiman, 2005](#); [Day et al., 2006](#); [Imae and Ikeda, 2007](#);

[Udry et al., 2012](#); [McCubbin et al., 2013](#); [Richter et al., 2014](#); [Jambon et al., 2016](#); [Richter et al., 2016](#); [Balta et al., 2017](#)) and were then transported and erupted with nakhlite lavas; or, they formed in two stages of melt evolution – the first stage involving high degree silica-poor melts producing olivine, and a second stage yielding augite from an evolving silica-rich melt upon ascent ([Goodrich et al., 2013](#)).

Studies of nakhlites have documented a variable range of oxygen fugacities extending from QFM –4 to QFM +1.5 and suggested changes in oxygen fugacity accompanied their magmatic and post magmatic evolution ([Bunch and Reid, 1975](#); [Dyar et al., 2005](#); [Makishima et al., 2007](#); [Richter et al., 2008](#); [Rutherford and Hammer, 2008](#);

\* Corresponding author.

E-mail address: [jdottin@umd.edu](mailto:jdottin@umd.edu) (J.W. Dottin).

Treiman and Irving, 2008; McCanta et al., 2009; Szymanski et al., 2010; Richter et al., 2014). Nakhilites also preserve evidence for interactions between nakhilite melts and surface-derived materials: sulfide with anomalous sulfur-isotope signatures as a result of assimilation of surface-derived sulfur (Farquhar et al., 2007; Franz et al., 2014); Cl-rich amphibole due to Cl-rich fluid interaction (Sautter et al., 2006; McCubbin et al., 2013); and isotopically light lithium isotope compositions (1.8–5.2‰) that indicate the presence of crustal contaminants (Magna et al., 2015). Moreover, variable amounts of intercumulus phases formed after crystal-liquid segregation (Dyar et al., 2005; Day et al., 2006; Udry et al., 2012) and intercumulus phases of some nakhilites, such as those from the Miller Range of Antarctica (MIL 090030, MIL 090032, and MIL 090036), include abundant skeletal magnetite and silica-rich mesostasis indicative of high oxygen fugacities during the latest stages of their crystallization.

Geochemical and petrologic characteristics of nakhilites have prompted hypotheses about genetic relationships linking them. It is generally believed that the nakhilites derive from different positions within one or more stratigraphically-related flows (Mikouchi et al., 2003; Mikouchi et al., 2006; Richter et al., 2016; Balta et al., 2017; Cohen et al., 2017). The relative positions of various nakhilites within the nakhilite pile and the processes that generated differences in their chemical, isotopic, and mineralogical characteristics, including why some like the MIL pairs became oxidized enough to yield significant amounts of skeletal titanomagnetite as an intercumulus phase, are issues that have not been fully resolved.

Work drawing on cooling rate determinations has led to debate about the position of members of the nakhilite group within the pile. One school of thought orders the nakhilites from most quickly-cooled at the top of the flow (MIL 03346, NWA 817, and Y00593) to more slowly-cooled deeper in the flow (Nakhla, Governador Valdez, Lafayette, and NWA998) (Mikouchi et al., 2006). Richter et al. (2016) use a 1-D thermal cooling model to argue that positions at the top and the bottom of the flow both satisfy fast cooling rates for NWA 817 (0.2 °C/h) and MIL 03346 (1 °C/h). These authors discuss how a mechanism to drain the lava overlying the cumulate layer, such as by the flow breaching its topographical enclosure, is a requirement to allow for efficient heat transfer and cooling for a top-of-flow position. They also discuss how fast cooling of a location near the base of the flow requires a mechanism to transport lavas with ~80% phenocrysts to a cold surface beneath the flow to promote rapid cooling. Richter et al. (2016) argue thus that both locations are allowed, but that additional constraints are needed to distinguish between them. A recent study by Cohen et al. (2017) has added an alternate scenario, argued on the basis of Ar-ages, that the nakhilites come from several different flows in a volcanic pile. According to their age-based reconstruction, MIL 03346 would be lower in the pile than many other nakhilites, but only because it preserves a more ancient age. Considerations for cooling rates and proximity to flow boundaries would still hold, but in this case the parameterization would need to account for the thickness of each distinct flow.

Franz et al. (2014) provide another window into the relationships between nakhilites, arguing that sulfur isotope data for sulfides from the MIL nakhilites indicate a contribution of sulfur from Martian surface sulfates via assimilation and reduction processes that is seen to a lesser extent in other nakhilites they have analyzed. These authors suggest that sulfates were assimilated by an over-riding flow, reacted with the melt, and were reduced to form sulfide that precipitated as minerals. These authors imply a connection between assimilation and oxygen fugacity changes in the melt.

To determine whether sulfate assimilation can account for the oxygen fugacity required to stabilize the high abundance of magnetite observed in some nakhilites, we performed wavelength-dispersive spectroscopy (WDS) analyses of phases in MIL 090030, 090032, and 090136 (all studied in Franz et al. 2014), and combine these results with site assignments to determine the Fe<sup>3+</sup> content and oxygen fugacity. In addition, we conducted X-ray mapping of these meteorites to determine the modal abundance and the ratio of magnetite to iron sulfide in the MIL pairs. Finally we examined the scale of isotopic variability by carrying out in-situ sulfur isotope analyses of nakhilite sulfides using secondary ion mass spectrometry (SIMS) in thick sections of these MIL pairs.

The sulfur isotope data are used to place constraints on the amounts of sulfate that could have been converted to sulfide via assimilation and reduction. The constraints on sulfate amounts added were, in turn, used to constrain the stratigraphic position of MIL nakhilites. Our observed anomalous sulfide S-isotope compositions suggest the uptake of high amounts of sulfate of which we hypothesize is most likely to occur at the base of the flow from which these meteorites derive.

## 1.1. Sample description

One inch round polished thick sections of MIL 09003043, MIL 09003287, MIL 09013634 allocated by the Meteorite Working Group from the Antarctic meteorite collections were used for this study. These meteorites are paired with the MIL 03346 nakhilite. MIL 090030, 090032, and 090136 are paired with MIL 03346 on the basis of common recovery location, similarities in mineralogy, and the similar petrographic textures of cumulus and intercumulus phases (Day et al., 2006; Hallis and Taylor, 2011; Udry et al., 2012). MIL 03346 is highly oxidized (QFM +1.5; (Dyar et al., 2005); QFM +0.5 (Richter et al., 2008) where QFM refers to log  $f_{O_2}$  relative to the Quartz-Fayalite-Magnetite redox buffer) and contains high concentrations of intergranular crystals and interstitial glass (avg. ~24.1% by volume) within the mesostasis (Day et al., 2006; McCanta et al., 2009; Hallis and Taylor, 2011; Udry et al., 2012; Kuebler, 2013). The cumulus phases in all four MIL meteorites are euhedral-subhedral zoned olivine and zoned pyroxene grains with magnesium-rich cores and ferroan rims (Day et al., 2006; Udry et al., 2012). The intercumulus phases are hosted within a glassy matrix and include sodic plagioclase, silica, phosphates, pyroxene, skeletal titanomagnetite, and iron sulfides (Day et al., 2006; Hallis and

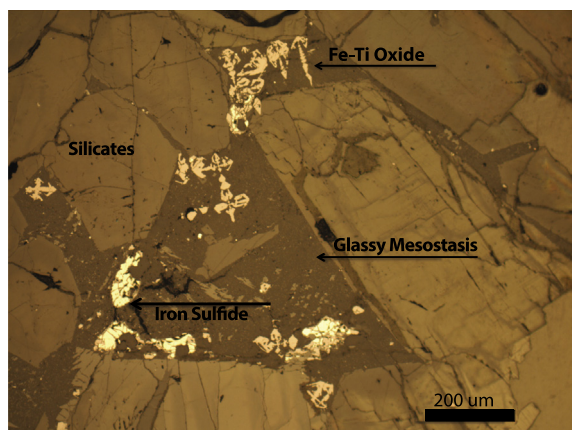


Fig. 1. Reflected light photomicrograph of intercumulus and cumulus phases for MIL 090136. The cumulus phases are predominantly pyroxene (light brown tabular crystals) and minor olivine (slightly darker brown equant crystals). The intercumulus portion consists of Fe-Ti oxide (skeletal titanomagnetite – cross shaped lightest brown) and iron sulfide (brassy) hosted within in a glassy mesostasis (darkest brown). Similar textures are noted for all MIL pairs. (For interpretation of the references to colour in this figure legend, the reader is referred to the web version of this article.)

Taylor, 2011; Udry et al., 2012). The skeletal titanomagnetite grains are predominantly hosted in the mesostasis (Fig. 1). In some cases, the titanomagnetite exists interstitial to the cumulus phases.

## 2. METHODS

### 2.1. Electron microprobe analyses

The compositions of pyroxene, olivine, and magnetite grains were determined by Electron Probe Micro Analyzer (EPMA) using the JEOL JXA-8900 Superprobe at the University of Maryland, College Park Advanced Imaging and Microscopy (AIM) Laboratory. Wavelength Dispersive Spectrometry (WDS) analyses were performed utilizing the accelerating potential of 15 kV, 10  $\mu\text{m}$  beam diameter, a 20 nA cup current, and a counting time of 20 s for iron and sulfur and 30 s for all other elements. Raw X-ray intensities were corrected with a ZAF (Z-atomic number correction, A-absorption correction, F-fluorescence correction) algorithm. The following standards were used for olivine analyses: San Carlos Olivine (Gila Co, AZ) USNM 111312/444 – Fe, Mg, Si, Ni; Kakanui Augite (New Zealand) USNM 122142–Ca, Al; Hypersthene (Johnstown Meteorite) USNM 746 – Cr; Fayalite (Rockport, MA) USNM 85276 – Mn; Kakanui Hornblende (New Zealand) USNM 143965 – Ti. The following standards were used for pyroxene analyses: Kakanui Hornblende (New Zealand) USNM 143965 – Fe, Ti Kakanui Augite (New Zealand) USNM 122142 – Ca, Mg, Al, Si; Fayalite (Rockport, MA) USNM 85276 – Mn; San Carlos Olivine (Gila Co, AZ) USNM 111312/444 – Ni; Hypersthene (Johnstown Meteorite) USNM 746 – Cr. For magnetite analyses, we used the following standards: Minas Gerais magnetite

USNM 114887 – Fe; Ilmen Mountains, Miask, USSR USNM 96189(1) – Ti, Mn; Kakanui Hornblende (New Zealand) – Ca, Mg, Al, Si; San Carlos Olivine (Gila Co, AZ) USNM 111312/444 Ni; Hypersthene (Johnstown Meteorite) USNM 746 – Cr. The following standards were used during sulfide analyses: Santa Eulalia Pyrrhotite USNM R7570 – Fe, S; Ellenville, NY, Chalcopyrite – Cu; Ni Metal – Ni; Co Metal – Co; Ilmen Mountains, Miask, USSR USNM 96189(1) – Mn, Ti. Site assignments and cation charge balance from EPMA data, were used to determine the  $\text{Fe}^{3+}$  content in magnetite according to the method of Droop (1987).

### 2.2. X-ray Mapping

X-ray maps were collected for the three Miller Range thick sections and were constructed using WDS grids for 5 elements: magnesium, calcium, iron, sulfur, and titanium. Spectral analyses were collected for 30 ms and each pixel was  $6.4 \times 6.4$  microns in area. Given the shape of the samples in thick section, the X-ray maps made for the MIL pairs were divided into multiple parts in order to maximize the area of the meteorite analyzed. Dimensions for the X-ray maps have been reported in Dottin, III (2016, MSc). Modal mineralogy maps for pyroxene, olivine, magnetite, sulfide, mesostasis were constructed with LISPIX (version LX190P) software using thresholds described in Dottin, III (2016, MSc).

### 2.3. Secondary Ion Mass Spectrometry (SIMS)

The thick sections were gold coated and then analyzed by secondary ion mass spectrometry (SIMS) to determine sulfur isotopes at the University of California, Los Angeles using a Cameca IMS 1270 multicollector ion microprobe. A total of 30 spots were analyzed among the three thick sections. Samples were sputtered with a 5 nA, 20 KeV  $\text{Cs}^+$  primary ion beam focused to a 15 micron spot. Charge compensation was performed using a normal-incidence electron flood gun. Each analysis spot was pre-sputtered for approximately 1.5–2 min followed by 30 cycles of analyses, with 10 seconds per cycle integration time. Secondary ions  $^{32}\text{S}^-$ ,  $^{33}\text{S}^-$ , and  $^{34}\text{S}^-$  were simultaneously collected using three Faraday cups (FCs) under mass resolving power ( $M/\Delta M$ ) of approximately 4000 and a 50 eV energy window. Data presented (Table 6) are normalized to Canyon Diablo Troilite (CDT) analyzed in the same session.

## 3. RESULTS

### 3.1. Elemental compositions

Major element compositions of representative pyroxene, olivine, titanomagnetite, and iron sulfides are reported in Tables 1–4. The complete data set with uncertainties for individual analyses is presented in the supplementary Tables 1–7. Fig. 2 illustrates compositional zoning for pyroxene and olivine that is most pronounced where the cumulate grains are in contact with the mesostasis. Pyroxene rims adjacent to mesostasis are depleted in Si, Mg and Cr, and enriched in Fe, Al and Ti. Olivine rims also

Table 1

Representative major element compositions for pyroxene in MIL 090136, MIL 090032, and MIL 090,030 and MIL 090,136.

wt%	MIL 090030- Px				MIL 090032- Px				MIL 090136- Px			
	Core	Rim adj. to mesostasis	Rim adj. to Px	Rim adj. to Ol	Core	Rim adj. to Ol	Rim adj. to Px	Rim adj. to Mesostasis	Core	Rim adj. to Ol	Rim adj. to Mesostasis	Rim adj. to Px
SiO <sub>2</sub>	51.93	47.66	51.83	52.1	52.41	52.41	51.79	47.48	52.02	51.3	51.09	50.89
Al <sub>2</sub> O <sub>3</sub>	0.93	3.71	0.94	1.12	0.89	0.95	1.21	4.01	0.93	0.92	1.33	1.39
TiO <sub>2</sub>	0.22	0.91	0.27	0.40	0.21	0.20	0.30	0.76	0.28	0.26	0.34	0.31
FeO	13.92	22.92	13.49	13.80	13.79	13.56	15.23	25.91	13.87	13.31	17.16	15.83
MgO	12.85	6.04	12.96	13.12	13.09	12.84	12.33	4.35	12.93	13.12	11.49	11.75
MnO	0.40	0.57	0.41	0.40	0.42	0.39	0.41	0.55	0.44	0.40	0.51	0.44
CaO	18.74	18.06	19.06	18.79	18.95	19.09	18.66	17.49	19.08	18.60	18.30	18.47
Cr <sub>2</sub> O <sub>3</sub>	0.46	0.00	0.34	0.37	0.29	0.37	0.18	0.00	0.35	0.37	0.09	0.14
NiO	0.00	0.00	0.00	0.00	0.00	0.02	0.00	0.00	0.00	0.02	0.00	0.00
Total	99.46	99.87	99.31	100.11	100.06	99.83	100.12	100.55	99.89	98.31	100.31	99.22
Fe <sub>2</sub> O <sub>3</sub>	0.00	0.00	0.00	0.00	0.00	0.00	0.00	0.00	0.00	0.00	0.23	0.00
FeO	13.92	22.92	13.49	13.80	13.79	13.56	15.23	25.91	13.87	13.31	16.95	15.83
Corrected total	99.46	99.87	99.31	100.11	100.05	99.83	100.11	100.55	99.89	98.31	100.33	99.22

Representative absolute uncertainties for analyses presented here are as follows: SiO<sub>2</sub> = 0.15, Al<sub>2</sub>O<sub>3</sub> = 0.02, TiO<sub>2</sub> = 0.02, FeO = 0.07, MgO = 0.07, MnO = 0.03, CaO = 0.07, Cr<sub>2</sub>O<sub>3</sub> = 0.03, and NiO = 0. Relative uncertainties for elemental compositions on each individual grain are presented in the supplementary information along with the elemental compositions.

Table 2

Representative major element compositions for olivine grains in MIL 090030, MIL 090032, and MIL 090,136.

	MIL 090030-Ol				MIL 090032-Ol			MIL 090136-Ol		
	Core	Rim adj. to altered Ol rim	Altered rim	Rim adj. to Px	Core	Rim adj. to Px	Rim adj. to mesostasis	Core	Rim adj. to Px	Rim adj. to mesostasis
SiO <sub>2</sub>	34.28	33.99	31.80	34.12	34.30	33.91	31.19	34.13	33.82	30.92
Al <sub>2</sub> O <sub>3</sub>	0.01	0.03	0.06	0.01	0.01	0.01	0.01	0.05	0.00	0.02
TiO <sub>2</sub>	0.00	0.00	0.02	0.01	0.00	0.00	0.11	0.00	0.00	0.01
FeO	44.74	46.30	56.50	44.50	45.35	45.64	60.08	45.22	45.54	60.87
MgO	19.94	18.15	9.04	19.71	19.87	17.80	5.62	19.60	19.32	5.76
MnO	0.89	0.99	1.41	0.90	0.93	0.90	1.51	0.96	0.95	1.59
CaO	0.56	0.54	0.52	0.55	0.59	0.50	0.15	0.54	0.59	0.30
Cr <sub>2</sub> O <sub>3</sub>	0.00	0.00	0.02	0.02	0.00	0.00	0.00	0.01	0.01	0.00
NiO	0.01	0.01	0.00	0.02	0.01	0.00	0.00	0.059	0.057	0.021
Total	100.43	100.02	99.37	99.84	101.07	98.76	98.66	100.56	100.30	99.50
Fe <sub>2</sub> O <sub>3</sub>	0.00	0.00	0.00	0.00	0.32	0.00	0.00	0.16	0.65	0.00
FeO	44.74	46.30	56.50	44.50	45.06	45.64	60.08	45.08	45.96	60.87
Corrected Total	100.43	100.02	99.37	99.84	101.10	98.76	98.66	100.57	100.37	99.50

Representative absolute uncertainties for analyses presented here are as follows: SiO<sub>2</sub> = 0.12, Al<sub>2</sub>O<sub>3</sub> = 0.01, TiO<sub>2</sub> = 0.02, FeO = 0.13, MgO = 0.10, MnO = 0.03, CaO = 0.02, Cr<sub>2</sub>O<sub>3</sub> = 0.02, and NiO = 0.03. Relative uncertainties for elemental compositions on each individual grain are presented in the supplementary information along with the elemental compositions.

Table 3

Representative major element compositions for magnetite grains in MIL 090030, MIL 090032, and MIL 090136.

MIL 090030-Mt			MIL 090032-Mt		MIL 090136-Mt	
Elongated			With SIMS spot		Adjacent to Px	
SiO <sub>2</sub>	0.21	0.26	0.21	0.25	0.24	0.27
Al <sub>2</sub> O <sub>3</sub>	2.12	0.35	2.83	3.05	2.79	1.94
TiO <sub>2</sub>	18.69	0.70	11.31	13.78	18.52	19.24
FeO	70.98	89.41	77.37	74.80	71.14	70.43
MgO	0.17	0.05	0.13	0.15	0.15	0.20
MnO	0.69	0.13	0.41	0.52	0.60	0.71
CaO	0.02	0.04	0.07	0.13	0.09	0.05
Cr <sub>2</sub> O <sub>3</sub>	0.01	0.00	0.02	0.02	0.00	0.00
NiO	0.00	0.00	0.00	0.00	0.00	0.00
Total	92.89	90.93	92.35	92.71	93.53	92.83
Fe <sub>2</sub> O <sub>3</sub>	26.95	64.87	40.94	35.72	26.88	25.87
FeO	46.73	31.04	40.53	42.66	46.96	47.15
Corrected Total	95.59	97.42	96.45	96.28	96.22	95.42

Elongated-This description refers to a grain that is seemingly much longer and less skeletal in its texture. Representative absolute uncertainties for analyses presented here are as follows: SiO<sub>2</sub> = 0.10, Al<sub>2</sub>O<sub>3</sub> = 0.04, TiO<sub>2</sub> = 0.09, FeO = 0.15, MgO = 0.10, MnO = 0.02, CaO = 0.03, Cr<sub>2</sub>O<sub>3</sub> = 0.02, and NiO = 0.02. Relative uncertainties for elemental compositions on each individual grain are presented in the supplementary information along with the elemental compositions.

Table 4

Representative major element compositions for iron sulfide grains in MIL 090030, MIL 090032, and MIL 090136.

Iron sulfide -	MIL 090030	MIL 090032	MIL 090136
Fe	61.30	59.74	60.79
Ni	0.02	0.00	0.00
S	38.93	39.15	38.91
Co	0.09	0.13	0.14
Cu	0.00	0.02	0.01
Ti	0.05	0.18	0.04
Mn	0.03	0.01	0.01
Total	100.43	99.23	99.90

Absolute uncertainty on Fe and S wt% compositions are  $\pm 0.21$  and  $\pm 0.08$  respectively.

display enrichments in Fe, Ti and Mn. The Fe is highest for the rims of both minerals adjacent to mesostasis (see [Tables 1 and 2](#), supplementary Tables 1 and 2, and [Fig. 2](#)). The characteristics of the olivine and pyroxene grains analyzed and reported here are similar to that reported in [Udry et al. \(2012\)](#), [Hallis and Taylor \(2011\)](#) (for MIL 090030, MIL 090032, and MIL 090136), [Imae and Ikeda \(2007\)](#), and [Day et al. \(2006\)](#) (for the paired meteorite MIL 03346).

The titanomagnetite in the MIL pairs range from a pure magnetite composition to ulvöspinel-rich compositions (Usp.  $\sim 0$  to Usp.  $\sim 65$  – [Table 3](#)). Titanomagnetite in sections of the three meteorites exhibit fine lamellar exsolution of ilmenite ([Fig. 3](#)). These compositions extend a wider range than that reported by [Udry et al. \(2012\)](#) (Usp. 33 to Usp. 65) on MIL 090030, MIL 090032, MIL 090136, and is more consistent with that reported by [Day et al. \(2006\)](#) on MIL 03346. EPMA analysis totals for titanium-rich magnetite from MIL 090030, MIL 090032, and MIL 090136 range from 95.4% to 98.2% (average: 96.4%) and are lower than totals reported in [Udry et al. \(2012\)](#). We have not been successful in identifying the reason for the low totals of our

analyses, but suggest that they may reflect complications arising because of surface topography, the carbon coating, or earlier gold coating. We do not think that a maghemite component or the presence of ilmenite (lamellae) in the analysis volume provides a viable explanation for this.

[Table 4](#) demonstrates that the iron sulfides most closely resemble data for pyrrhotite (Fe<sub>(1-x)</sub>S, where  $x = 0-0.17$ ). The average iron sulfide compositions for MIL 090030, MIL 090032, and MIL 090136 are Fe<sub>0.90</sub>S, Fe<sub>0.89</sub>S, and Fe<sub>0.89</sub>S respectively. The sulfide compositions are similar to that observed by [Udry et al. \(2012\)](#) (with the exception of MIL 090030) who report Fe<sub>1.1</sub>S, Fe<sub>0.92</sub>S, and Fe<sub>0.91</sub>S compositions for MIL 090030, MIL 090032, and MIL 090136 respectively, observations by [Hallis and Taylor \(2011\)](#) who report Fe<sub>0.95</sub>S and Fe<sub>0.90</sub>S, Fe<sub>0.96</sub>S, and Fe<sub>0.94</sub>S compositions for MIL 090030, MIL 090032, and MIL 090136 respectively, and that reported MIL 03346 by [Day et al., 2006](#) and [Imae and Ikeda \(2007\)](#) who report a Fe<sub>0.87</sub>S composition.

### 3.2. Modal Abundances

Modal abundances of pyroxene, olivine, mesostasis, magnetite, and sulfide for the three studied sections are presented in [Table 5](#). We have calculated the modes of the main phases as well as the relative proportions of cores and rims in the olivine and pyroxene phenocrysts. Three phase maps are displayed in [Fig. 4](#). The three sections reveal variations in modal abundance of pyroxene (60–71%), olivine (1–9%), mesostasis (22–32%), magnetite (1.83–1.93%) and sulfide (0.06–0.23%). The modes reported here are similar to that observed by [Udry et al. \(2012\)](#) and [Hallis and Taylor \(2011\)](#) who report 64–75% pyroxene, 3.0–9.5% olivine, 0.6–2.0% magnetite, and 18.1–26.4% intercumulus matrix (mesostasis) in MIL 090030, 090032, and 090136. [Day et al. \(2006\)](#) and [Imae and Ikeda \(2007\)](#) also report similar modes. MIL 090032 displays the lowest



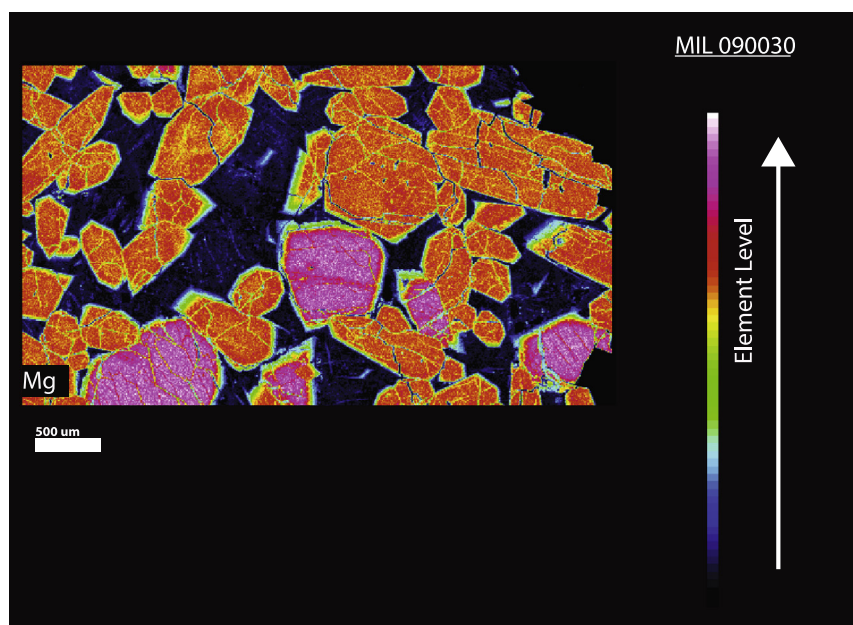


Fig. 2. A. WDS X-ray map of magnesium in MIL 090030. Pyroxene is red/orange; olivine is purple, and mesostasis is dark. The image illustrates Mg depletion in the rims of pyroxene and olivine grains that is most pronounced where they contact mesostasis.

concentration of olivine and sulfide by an order of magnitude. Uncertainty on modal estimates for the individual sections was calculated using the method of [van der Plas and Tobi \(1965\)](#). Uncertainties applied to these modal estimates within paired samples are larger than that presented because our data do not capture variations that occur on scales greater than the individual sections. The compositional and modal data for iron sulfide in combination with the density of 3.4 g/cc for these meteorites ([Macke et al., 2011](#)), yields estimated S concentrations of  $310 \pm 10$  ppm S for the section of MIL 090032 and  $1180 \pm 50$  ppm S for the sections of MIL 090030 and MIL 090136 (uncertainty determined using monte carlo error propagation).  $\text{Fe}^{3+}$  for these sections is determined using modal data in combination with the major element compositions of the phases and proportions of cores and rims for olivine and pyroxene.  $\text{Fe}^{3+}$  is estimated to be 0.85 wt%, 0.67 wt%, 0.81 wt% for our sections of MIL 090030, MIL 090032, and MIL 090136 respectively.

### 3.3. Secondary ion mass spectrometry analyses

Sulfur isotope data for iron sulfide grains in the three MIL sections is presented in [Table 6](#). The average  $\delta^{34}\text{S}$  for MIL 090136, MIL 090032, and MIL 090030 are  $14.3 \pm 1.3\text{‰}$ ,  $14.7 \pm 3.0\text{‰}$ , and  $13.7 \pm 2.8\text{‰}$  (1 S.D.), respectively. The average  $\Delta^{33}\text{S}$  for these samples are  $-0.68 \pm 0.14\text{‰}$ ,  $-0.60 \pm 0.06\text{‰}$ , and  $-0.76 \pm 0.15\text{‰}$  (1 S.D.) for MIL 090136, MIL 090032, and MIL 090030 respectively. Given the number of samples analyzed, the scatter in these analyses given by the population standard deviation are not sufficiently greater than the analytical uncertainties to argue conclusively that they resolve internal isotopic heterogeneity. This assumes that there is

uncertainty on the standard deviation that scales with  $\sigma/(2n)^{1/2}$  ([Dietrich, 1991](#)). [Fig. 5](#) compares average values of our SIMS analyses of the MIL pairs with acid extractions of whole meteorite sulfur and SIMS analyses for nakhlites reported in the prior study by [Franz et al. \(2014\)](#) and [Farquhar et al. \(2000, 2007\)](#). Analyses of these three meteorites using chemically extracted sulfur and the  $\text{SF}_6$  gas source isotope ratio method performed by [Franz et al. \(2014\)](#) yielded less positive  $\delta^{34}\text{S}$  (average difference with our data is  $5.8 \pm 0.2\text{‰}$ ) and less negative  $\Delta^{33}\text{S}$  outside of 2  $\sigma$  for MIL 090,030 (absolute value of  $-0.538 \pm 0.008\text{‰}$ , compared to our  $-0.68 \pm 0.14\text{‰}$ ), MIL 090,032 ( $-0.523 \pm 0.008\text{‰}$  compared to our  $-0.60 \pm 0.06\text{‰}$ ), and MIL 090,136 ( $-0.476 \pm 0.008\text{‰}$  compared to  $-0.76 \pm 0.15\text{‰}$ ).

## 4. DISCUSSION

### 4.1. Isotope evidence for sulfur addition

[Franz et al. \(2014\)](#) argue that the negative  $\Delta^{33}\text{S}$  and positive  $\delta^{34}\text{S}$  of sulfide in the MIL pairs, relative to sulfide from other Martian meteorites, reflect assimilation and reduction of sulfate sulfur by nakhlite magmas. Negative  $\Delta^{33}\text{S}$  has been reported by [Farquhar et al. \(2007\)](#) for sulfate from Nakhla and was used by [Franz et al. \(2014\)](#) to constrain the signature of the assimilated Martian sulfate, which would ultimately have been produced by mass-independent Martian atmospheric chemistry. Since the  $\Delta^{33}\text{S}$  varies among nakhlites, the amounts of sulfur added to different nakhlites also varied, raising the possibility of a relationship to position within the nakhlite pile – for instance, proximity to either the upper or lower flow surface.

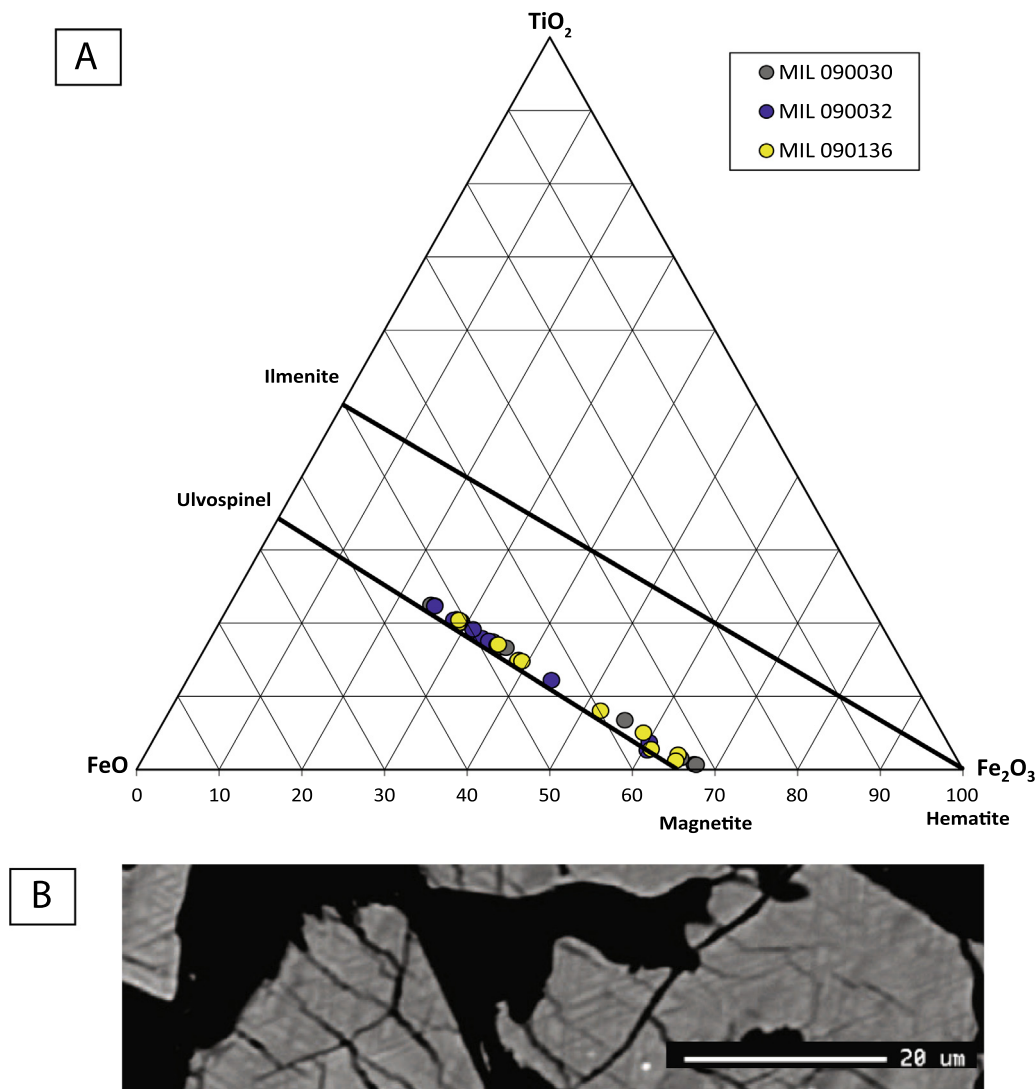


Fig. 3. (A) Spinel ternary diagram illustrating the range of titanomagnetite compositions. The most ulvöspinel-rich components are interpreted to represent preservation of the highest temperature equilibrated compositions, and the more magnetite-rich compositions are interpreted to reflect equilibration at lower temperatures. Note our data plot above the tie line for ulvöspinel and magnetite, which indicate the possible presence of ilmenite and/or maghemite. Such presence of the phases may also be the cause for the low totals (Table 3). (B) Back Scatter Electron image of intercumulus magnetite with exsolution lamellae in the MIL 090030 meteorite. This feature is seen in all of the magnetite grains in the MIL pairs.

Table 5  
Calculated modes of major phases in volume % for MIL 090030, MIL 090032, and MIL 090,136.

Sample	Total Pixels	Pyroxene	Olivine	Mesostasis	Magnetite	Sulfide
MIL 090030	656,000	66.6	8.8	22.5	1.9	0.2
( $\pm$ %)		0.06	0.03	0.05	0.02	0.01
MIL 090032	650,000	71.0	1.0	26.1	1.9	0.1
( $\pm$ %)		0.06	0.01	0.05	0.02	0.00
MIL 090136	1,500,000	60.7	4.9	32.3	1.8	0.2
( $\pm$ %)		0.04	0.02	0.04	0.01	0.00

Uncertainties are reported as absolute  $2\sigma$

Constraints on the distribution of anomalous sulfur within the flow are needed to explore the amount of sulfur that may have been added in total. Based on cooling rates

determined via lithium zoning of augite and olivine grains, Richter et al. (2016) place MIL 03346 at approximately 0.75 m from either the top or bottom surface of the flow.

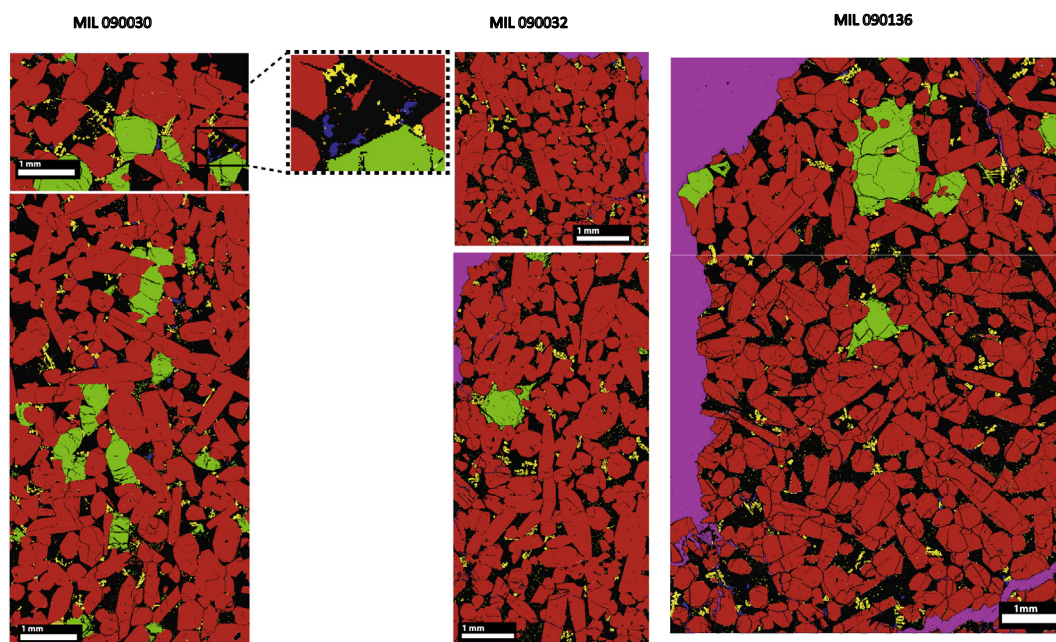


Fig. 4. Modal abundance maps constructed using LISPIX for MIL pairs studied here. These maps are constructed using X-ray compositional maps that have been processed in LISPIX in order to determine the modal mineralogy. The image highlights pyroxene (red), olivine (green), titanomagnetite (yellow), and sulfide (blue). Phases were characterized using Fe, Mg, Ca, S, and Ti. See (Dottin III, 2016, [M.sc](#)) section for details on the technique. (For interpretation of the references to colour in this figure legend, the reader is referred to the web version of this article.)

Since MIL 03346 is paired with the meteorites studied here, we explore the possibility that a similar amount of sulfur would have been added over the entire 0.75 m. Assuming the added sulfur had a  $\Delta^{33}\text{S}$  like that seen in the most negative sulfate from Martian meteorites ( $\Delta^{33}\text{S} = -1.25 \pm 0.01\text{‰}$ ; Farquhar et al. (2007)), the  $\Delta^{33}\text{S}$  of the MIL sulfides ( $\sim -0.6$  to  $-0.76\text{‰}$ ) suggests that approximately 50–60% of the sulfur presently in these meteorites, and by extension, the outer  $\sim 0.75$  m of the flow, came from the assimilation (and reduction) of such sulfate.

We consider two endmember scenarios to constrain upper and lower limits on the amount of added sulfate sulfur. For the upper bound, assimilated sulfate sulfur is mixed with juvenile sulfur having a concentration determined by sulfide saturation ( $\sim 2000$  ppm; Chevrier et al., 2011), and would imply addition of a similar amount into the lower 0.75 m of the flow. The abundance of sulfide presently observed, however, is  $\sim 1300$  ppm for MIL 090030 and MIL 090136 (360 ppm for MIL 09032). These low S contents compared to the prediction above could imply that degassing or weathering occurred during and/or after the solidification of the nakhlite flow. A lower bound is constrained assuming the concentrations of sulfide presently observed in the meteorites include both the juvenile and assimilated sulfur without degassing and/or weathering, and imply addition of only 170–800 ppm of sulfur from sulfate to the lower 0.75 m of the flow. The necessary sulfur is significant, and would represent the equivalent amount of sulfate contained in 1–10 cm of Martian regolith/soil with 6 wt%  $\text{SO}_3$  (O’Connell-Cooper et al., 2017). More material would be required for the upper-bound endmember

scenario, which adds the equivalent of 2000 ppm of sulfur to the lower 1–2 m of the flow. We see no reasonable way to deposit this amount of sulfur on top of a nakhlite flow at the of emplacement. This finding alone, leads us to suggest that the MIL pairs either occupied a position at the base of a large flow, and the amounts of sulfur added to higher portions of the flow were lower, or that the MIL pairs came from a specific flow (model of Cohen et al., 2017) that interacted with more sulfur-rich Martian sediment than did other nakhlite flows.

#### 4.2. The role of sulfate as an oxidizing agent

We observe high amounts of  $\text{Fe}^{3+}$  in the MIL pairs (0.81 wt%, 0.85 wt%, and 0.67 wt% for MIL 090136, MIL 090030, and MIL 090032 respectively, see Section 3.2) with most  $\text{Fe}^{3+}$  hosted within titanomagnetite. Dyar et al. (2005) report an oxygen fugacity of QFM +1.5 for MIL 03346. McCanta et al. (2009) estimate a lower oxygen fugacity (using a Eu-oxybarometer) of QFM +1 for MIL 03346 measured in pyroxenes. Hallis and Taylor (2011) describe a mesostasis assemblage with cristobalite and titanomagnetite, which is also consistent with an oxygen fugacity near or exceeding QFM (see also Rutherford and Hammer, 2008) compared to other nakhlites: NWA 998 (QFM  $-0.8$ ), Y-000593 (QFM  $-0.7$ ), Nakhla (QFM) and Lafayette (QFM +0.1) (Dyar et al., 2005; McCanta et al., 2009; Szymanski et al., 2010). For MIL 090030, MIL 090032, and MIL 090136, the relatively high  $\text{Fe}^{3+}$  implies high oxygen fugacity at the time the flows were emplaced. Considering the most ulvöspinel-rich compositions (Fig. 3), the least



Table 6  
SIMS data corrected to Anderson Pyrrhotite.

Sample	$\delta^{34}\text{S}$ 1 $\sigma^a$	$\Delta^{33}\text{S}$ 1 $\sigma^a$
MIL 090136-4	14.4 $\pm$ 0.06	−0.72 $\pm$ 0.04
MIL 090136-5	18.3 $\pm$ 0.08	−0.96 $\pm$ 0.05
MIL 090136-10	18.4 $\pm$ 0.05	−0.92 $\pm$ 0.12
MIL 090136-11	11.2 $\pm$ 0.04	−0.84 $\pm$ 0.07
MIL 090136-12	14.0 $\pm$ 0.19	−0.64 $\pm$ 0.06
MIL 090136-13	10.4 $\pm$ 0.09	−0.88 $\pm$ 0.06
MIL 090136-14	15.1 $\pm$ 0.04	−0.88 $\pm$ 0.04
MIL 090136-15	12.0 $\pm$ 0.10	−0.66 $\pm$ 0.07
MIL 090136-16	14.1 $\pm$ 0.11	−0.50 $\pm$ 0.07
MIL 090136-19	11.0 $\pm$ 0.13	−0.58 $\pm$ 0.08
MIL 090136-21	11.6 $\pm$ 0.10	−0.81 $\pm$ 0.08
Average	13.7 $\pm$ 2.74	−0.76 $\pm$ 0.15
MIL 090032-1	15.3 $\pm$ 0.09	−0.65 $\pm$ 0.07
MIL 090032-2	11.7 $\pm$ 0.10	−0.65 $\pm$ 0.05
MIL 090032-3	14.3 $\pm$ 0.03	−0.53 $\pm$ 0.06
MIL 090032-4	12.7 $\pm$ 0.22	−0.63 $\pm$ 0.07
MIL 090032-5	19.4 $\pm$ 0.09	−0.53 $\pm$ 0.07
Average	14.7 $\pm$ 2.92	−0.60 $\pm$ 0.06
MIL 090030-1	14.4 $\pm$ 0.47	−0.66 $\pm$ 0.06
MIL 090030-2	15.4 $\pm$ 0.44	−0.71 $\pm$ 0.05
MIL 090030-3	14.6 $\pm$ 0.39	−0.82 $\pm$ 0.08
MIL 090030-4	16.9 $\pm$ 0.26	−0.53 $\pm$ 0.10
MIL 090030-5	13.3 $\pm$ 0.18	−0.66 $\pm$ 0.08
MIL 090030-6	15.1 $\pm$ 0.33	−0.32 $\pm$ 0.05
MIL 090030-7	13.2 $\pm$ 0.42	−0.67 $\pm$ 0.06
MIL 090030-8	13.9 $\pm$ 0.29	−0.79 $\pm$ 0.06
MIL 090030-9	14.5 $\pm$ 0.24	−0.79 $\pm$ 0.08
MIL 090030-10	14.1 $\pm$ 0.24	−0.77 $\pm$ 0.06
MIL 090030-12	14.6 $\pm$ 0.20	−0.66 $\pm$ 0.08
MIL 090030-13	11.7 $\pm$ 0.18	−0.78 $\pm$ 0.07
Average	14.3 $\pm$ 1.25	−0.68 $\pm$ 0.14

<sup>a</sup> The uncertainty presented reflects the uncertainty on the analyses for individual spot grains. The uncertainty reported for the average is the 1 sigma standard deviation of the analyses of a given meteorite.

ferroan olivine (cores), and the most ferroan augite (cores), the Fayalite-Augite-Magnetite oxybarometer (Andersen et al., 1993; QUILF version 6.42) yields  $\sim$  QFM  $-0.1$  between 1000 and 1200 °C. This oxygen fugacity is below saturation of SiO<sub>2</sub> for the measured ulvöspinel, olivine, and augite compositions (QFM  $+0.3$  to  $+0.7$ ; calculated with the same program). The measured olivine, augite, and ulvöspinel compositions yield SiO<sub>2</sub> saturation at somewhat lower temperatures,  $\sim$ 850 °C, calculated using Andersen et al. (1993).

The crystallization and exsolution of titanomagnetite extended from slightly above the solidus, well into the subsolidus cooling history of the flow. Richter et al. (2008) and Richter et al. (2013) argue that Ti magnetite would not be a liquidus phase for Martian melt  $f_{\text{O}_2}$  buffered by C-H-O equilibria (QFM  $+1$  to QFM-3), and Rutherford and Hammer (2008) demonstrate that magnetite is stabilized near the solidus at oxygen fugacity of QFM. Hallis and Taylor (2011) argue that magnetite textures in the MIL pairs call for crystallization from melt (above the solidus),

including significant crystallization during the rapid cooling that produced the mesostasis. Richter et al. (2014) document significant subsolidus re-equilibration of Fe-Ti oxides for MIL 03346 on cooling which drove oxygen fugacity to very low values (QFM  $-4$ ) by the time the rocks cooled to  $\sim$ 200 °C. We show evidence of similar down temperature equilibration of Fe-Ti oxides in the MIL pairs studied here as compositional arrays extending from ulvöspinel to magnetite (Fig. 5). This evolution is supported by exsolution of ilmenite, evidence of which is present in titanomagnetite from all examined sections (Fig. 5). Thus while stabilization of magnetite required a high oxygen fugacity at the time of crystallization, the subsolidus evolution of magnetite complicates understanding the precise oxygen fugacity that prevailed.

We explore another potential link between sulfate and titanomagnetite by considering the extent to which sulfate addition and reduction could account for the oxidation by considering the following endmember reactions:

- (1)  $13\text{FeSiO}_3 + \text{CaSO}_4 \rightleftharpoons \text{FeS} + 4\text{Fe}_3\text{O}_4 + \text{CaSiO}_3 + 12\text{SiO}_2$
- (2)  $13\text{Fe}_2\text{SiO}_4 + 2\text{CaSO}_4 \rightleftharpoons 2\text{FeS} + 8\text{Fe}_3\text{O}_4 + \text{Ca}_2\text{SiO}_4 + 12\text{SiO}_4$
- (3)  $55\text{FeSiO}_3 + 2\text{KFe}_3(\text{OH})_6(\text{SO}_4)_2 \rightleftharpoons 4\text{FeS} + 19\text{Fe}_3\text{O}_4 + 55\text{SiO}_2 + \text{K}_2\text{O} + 6\text{H}_2\text{O}$ , and
- (4)  $55\text{Fe}_2\text{SiO}_4 + 4\text{KFe}_3(\text{OH})_6(\text{SO}_4)_2 \rightleftharpoons 8\text{FeS} + 38\text{Fe}_3\text{O}_4 + 55\text{SiO}_2 + 2\text{K}_2\text{O} + 12\text{H}_2\text{O}$ .

The first two reactions yield 13.9 times more Fe<sup>3+</sup> in magnetite by mass than S<sup>2−</sup> in pyrrhotite, and the second two reactions yield 16.6 times more Fe<sup>3+</sup> in magnetite by mass than S<sup>2−</sup> in pyrrhotite. The limits described above for the addition of an amount of sulfur equivalent to 500–2000 ppm would account for an Fe<sup>3+</sup> concentration between 0.7 and 3.5 wt%, which overlaps with the observed Fe<sup>3+</sup> in the MIL pairs (0.67–0.85 wt%) at its lower end. This finding implies that alternative oxidizing agents such as perchlorate (7 e<sup>−</sup>), chlorate (5 e<sup>−</sup>), nitrate (5 e<sup>−</sup>), or hydrogen peroxide (2 e<sup>−</sup>) were not required (Chevrier and Mathé, 2007; Kounaves et al., 2014; Dehouck et al., 2016), however, this, and the possible deficit for Fe<sup>3+</sup> can be accounted for with addition of lesser amounts of sulfur having more negative  $\Delta^{33}\text{S}$  than the sulfate from Nakhla,  $-1.25\text{‰}$  (Farquhar et al., 2007).

Several other Nakhilites also show sulfides with lower level anomalous  $\Delta^{33}\text{S}$  suggesting they also acquired sulfur ultimately derived from such a source such as photolytic sulfate. Not all of these exemplars exhibit the same spectacular Fe-Ti oxides as the MIL pairs, suggesting that sulfate may have been reduced to sulfide that migrated from one part of the flow to another shifting the sulfur isotopic compositions by a small amount in areas of the flow where the production of titanomagnetite by reactions like (1–4) did not occur. For some meteorites, like Nakhla, evidence for later addition of sulfur during Martian weathering is preserved by the presence of sulfate with nonzero  $\Delta^{33}\text{S}$  and  $\Delta^{17}\text{O}$  (Farquhar and Thieme, 2000; Farquhar et al., 2007).

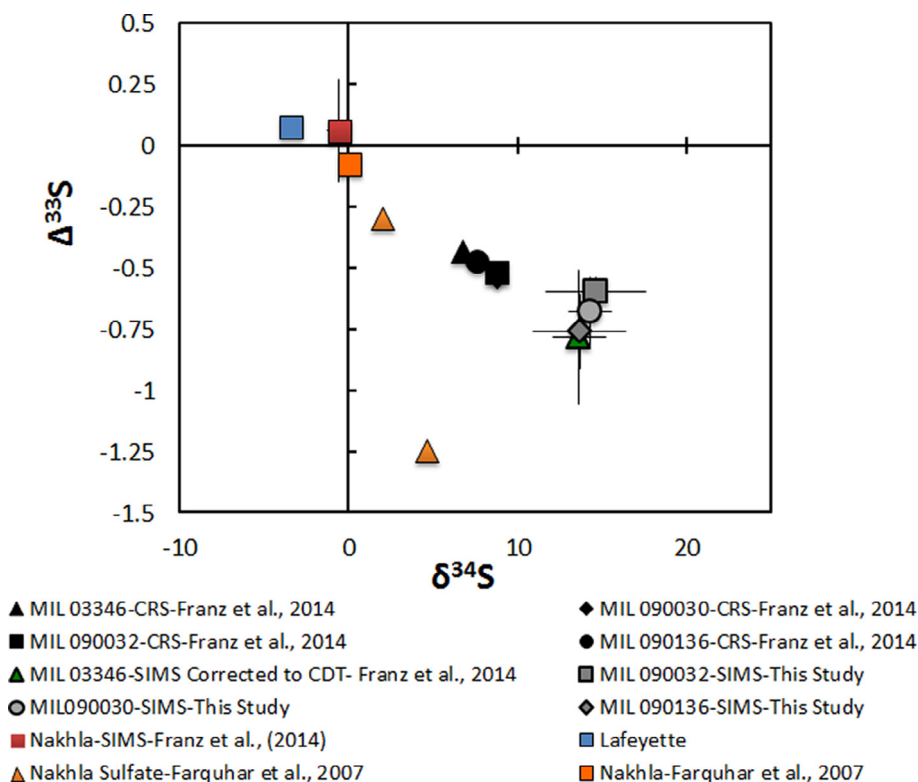


Fig. 5. Plot of  $\delta^{34}\text{S}$  vs.  $\Delta^{33}\text{S}$  for average values from SIMS analyses of MIL 090030/090032/09013 (grey symbols) along with published analyses for other nakhlites. Note that the sulfur isotopic compositions measured by SIMS analyses presented here and in Franz et al. (2014) plot further along the array defined by the sulfide data (more positive  $\delta^{34}\text{S}$  vs. and negative  $\Delta^{33}\text{S}$ ) than the conventional acid extractions (black symbols for same meteorites). The origin of this shift is unclear, but it is possible that the SIMS is capturing sulfide with a greater contribution from assimilated sulfur.

#### 4.3. Positive $\delta^{34}\text{S}$

The average  $\delta^{34}\text{S}$  for MIL 090030, MIL 090032, and MIL 090136 are  $13.7 \pm 2.8\text{‰}$  (1 S.D.),  $14.7 \pm 3.0\text{‰}$ , and  $14.3 \pm 1.3\text{‰}$  respectively (see Table 6). These  $\delta^{34}\text{S}$  values are positive relative to the sulfate observed in Nakhla ( $4.7\text{‰}$ , Farquhar et al., 2007). This observation may implicate additional processes associated with the reduction of the assimilated sulfate. Isotope fractionation by both equilibrium and kinetic effects can enrich the heavy isotopes (e.g.,  $^{34}\text{S}$ ) as a result of preferential loss of the lighter isotope (e.g.,  $^{32}\text{S}$ ) during magmatic degassing of sulfur bearing gases. Such a process has been well documented for oxidized terrestrial melts when  $\text{H}_2\text{S}$  and  $\text{SO}_2$  are degassed while sulfur remains in the melt as  $\text{SO}_4^{2-}$  and/or  $\text{S}^{2-}$  (Labidi et al., 2015; Mandeville et al., 2009). Here, both  $\text{SO}_2$  or  $\text{H}_2\text{S}$  loss under equilibrium or kinetic degassing, while sulfur was under the form of  $\text{SO}_4$  in the melt, would favor the partitioning of light S isotopes in the vapor phase. We suggest that degassing occurred while the process of  $\text{SO}_4$  reduction was ongoing, shifting the residual  $\text{SO}_4$  to more positive  $\delta^{34}\text{S}$ . Subsequent reduction of this residual  $\text{SO}_4$  then allowed the formation of sulfide as observed in the MIL pairs.

The suggestion of degassing is not new. Righter et al. (2014) argue that S degassing would result in S-loss at the

top of the flow, and that those meteorites with the lowest S contents likely occupied the uppermost positions in the flow. Our data, along with that reported by Franz et al. (2014), suggest that the MIL pairs record higher S concentrations (as S ppm) than other nakhlites suggesting the MIL pairs would have experienced less degassing than other nakhlites, providing possibly another indirect constraint on the position within their respective flows.

#### 4.4. A note on alteration and terrestrial weathering

Work by Hallis and Taylor (2011) present evidence for alteration and terrestrial oxidation via Antarctic fluids, and it is clear that similar evidence is also present in the samples we examined, but we do not think this provides an alternative way to explain our observations. Work by Franz et al. (2014) demonstrated that the sulfate from MIL pairs also possessed sulfate with slightly less negative  $\Delta^{33}\text{S}$  and slightly more positive  $\delta^{34}\text{S}$  relative to coexisting sulfide minerals and different from the composition of sulfate from the Nakhla, which was recovered shortly after it fell (Farquhar et al., 2007). We attribute these isotopic compositions of sulfate to mixing of sulfur produced by terrestrial oxidation of indigenous sulfide minerals with terrestrial sulfate. Given the evidence for such terrestrial alteration reactions, the sulfide abundances below sulfide saturation (2000 ppm) likely

in part also reflect terrestrial weathering. However, this terrestrial alteration is not expected to alter the  $\Delta^{33}\text{S}$  or  $\delta^{34}\text{S}$  of the remaining sulfide minerals, and thus does not impact the hypotheses we propose.

## 5. SUMMARY

We present new sulfur isotope data, mineral compositions, modal abundance data, and petrographic details on MIL 090030, MIL 090032, and MIL 090136. Overall, this analysis suggests that the reduction of sulfate from the Martian surface, coupled with the oxidation of  $\text{Fe}^{2+}$ , played a significant role in the late magmatic evolution of the MIL pairs, resulting in the stabilization of titanomagnetite and the high observed  $f\text{O}_2$ . Our S-isotope data for sulfide minerals show a negative  $\Delta^{33}\text{S}$  signature in the MIL pairs relative to Nakhla sulfide. The combination of this anomalous S-isotope signature, a significant amount of magnetite in the samples and the constraints by Richter et al. (2016) that place the samples approximately 0.75 m into the flow, provides evidence for assimilation of significant amounts of Martian surface sulfate (either as sediment or possibly as a brine) – equivalent to 1–10 cm of Martian regolith/soil with 6 wt%  $\text{SO}_3$  (O'Connell-Cooper et al., 2017). Given this amount of assimilated sulfate, we argue that the MIL pairs are more plausibly located near the base of a flow rather than near its top. Additionally, The smaller  $^{33}\text{S}$  depletions and lower oxygen fugacity in other nakhlites imply lesser amounts of added sulfur, but some such as Nakhla carry small anomalies (Farquhar et al., 2000, 2007; Franz et al., 2014), and it can be argued would also have been subject to this process.

## ACKNOWLEDGEMENTS

Associate editor Chris Herd and reviewer Brian Balta are thanked for their helpful and thoughtful comments. This work was funded by the NASA (NNX16AG39G and NNX12ZDA001N-COS), and Ronald E. McNair graduate fellowship program. We acknowledge the support of the Maryland NanoCenter and its AIMLab. The ion microprobe facility at UCLA is partially supported by a grant from the Instrumentation and Facilities Program, Division of Earth Sciences, National Science Foundation. Axel Schmitt is thanked for his help with sample preparation and analyses on the ion probe.

## APPENDIX A. SUPPLEMENTARY DATA

Supplementary data associated with this article can be found, in the online version, at <https://doi.org/10.1016/j.gca.2018.07.029>.

## REFERENCES

- Andersen D. J., Lindsley D. H. and Davidson P. M. (1993) QUILF: A pascal program to assess equilibria among Fe-Mg-Mn-Ti oxides, pyroxenes, olivine, and quartz. *Comput. Geosci.* **19**, 1333–1350.
- Balta J. B., Sanborn M. E., Mayne R. G., Wadhwa M., McSween H. Y. and Crossley S. D. (2017) Northwest Africa 5790: a previously unsampled portion of the upper part of the nakhlite pile. *Meteorit. Planet. Sci.* **52**, 36–59.
- Bunch T. E. and Reid A. M. (1975) The nakhlites Part I: Petrography and mineral chemistry. *Meteorit. Planet. Sci.* **10**, 303–315.
- Chevrier V., Lorand J. P. and Sautter V. (2011) Sulfide petrology of four nakhlites: Northwest Africa 817, Northwest Africa 998, Nakhla, and Governador Valadares. *Meteorit. Planet. Sci.* **46**, 769–784.
- Chevrier V. and Mathé P. E. (2007) Mineralogy and evolution of the surface of Mars: a review. *Planet. Space Sci.* **55**, 289–314.
- Cohen B. E., Mark D. F., Cassata W. S., Lee M. R., Tomkinson T. and Smith C. L. (2017) Taking the pulse of Mars via dating of a plume-fed volcano. *Nat. Commun.* **8**, 640.
- Day J. M. D., Taylor L. A., Floss C. and McSween H. Y. (2006) Petrology and chemistry of MIL 03346 and its significance in understanding the petrogenesis of nakhlites on Mars. *Meteorit. Planet. Sci.* **41**, 581–606.
- Dehouck E., Gaudin A., Chevrier V. and Mangold N. (2016) Mineralogical record of the redox conditions on early Mars. *Icarus* **271**, 67–75.
- Dietrich C. F. (1991) Uncertainty, calibration and probability. The statistics of scientific and industrial measurement. Adam Hilger.
- Dottin, III, J. W. (2016) *Assessing the oxidative history of Miller Range Martian meteorites*. University of Maryland, College Park. <https://doi.org/10.13016/M2MB8Q>, Masters Thesis.
- Droop T. R. (1987) A general equation for estimating  $\text{Fe}^{3+}$  concentrations in ferromagnesian silicates and oxides from microprobe analyses, using stoichiometric criteria. *Mineral. Mag.* **51**, 431–435.
- Dyar M. D., Treiman A. H., Pieters C. M., Hiroi T., Lane M. D. and O'Connor V. (2005) MIL03346, the most oxidized Martian meteorite: a first look at spectroscopy, petrography, and mineral chemistry. *J. Geophys. Res. Planets* **110**, 1–9.
- Farquhar J., Kim S. T. and Masterson A. (2007) Implications from sulfur isotopes of the Nakhla meteorite for the origin of sulfate on Mars. *Earth Planet. Sci. Lett.* **264**, 1–8.
- Farquhar J., Savarino J., Jackson T. L. and Thiemens M. H. (2000) Evidence of atmospheric sulphur in the martian regolith from sulphur isotopes in meteorites. *Nature* **404**, 50–52.
- Farquhar J. and Thiemens M. H. (2000) Oxygen cycle of the Martian atmosphere-regolith system:  $\Delta^{17}\text{O}$  of secondary phases in Nakhla and Lafayette. *J. Geophys. Res. Planets* **105**, 11991–11997.
- Franz H. B., Kim S.-T., Farquhar J., Day J. M. D., Economos R. C., McKeegan K. D., Schmitt A. K., Irving A. J., Hoek J. and Dottin J. (2014) Isotopic links between atmospheric chemistry and the deep sulphur cycle on Mars Available at: *Nature* **508**, 364–368.
- Goodrich C. A., Treiman A. H., Filiberto J., Gross J. and Jercinovic M. (2013)  $\text{K}_2\text{O}$ -rich trapped melt in olivine in the Nakhla meteorite: implications for petrogenesis of nakhlites and evolution of the Martian mantle. *Meteorit. Planet. Sci.* **48**, 2371–2405.
- Hallis L. J. and Taylor G. J. (2011) Comparisons of the four Miller Range nakhlites, MIL 03346, 090030, 090032 and 090136: textural and compositional observations of primary and secondary mineral assemblages. *Meteorit. Planet. Sci.* **46**, 1787–1803.
- Imae N. and Ikeda Y. (2007) Petrology of the Miller Range 03346 nakhlite in comparison with the Yamato-000593 nakhlite. *Meteorit. Planet. Sci.* **42**, 171–184.
- Makishima, J., McKay, G., Le, L., Miyamoto, M., Mikouchi, T., 2007. Oxidation state of nakhlites as inferred from Fe-Ti oxide equilibria and augite/melt europium partitioning. In 38th Lunar and Planetary science conference (abstract#1834).

- Jambon A., Sautter V., Barrat J. A., Gattacceca J., Rochette P., Boudouma O., Badia D. and Devouard B. (2016) Northwest Africa 5790: Revisiting nakhlite petrogenesis. *Geochim. Cosmochim. Acta* **190**, 191–212.
- Kounaves S. P., Carrier B. L., O’Neil G. D., Stroble S. T. and Claire M. W. (2014) Evidence of martian perchlorate, chlorate, and nitrate in Mars meteorite EETA79001: implications for oxidants and organics. *Icarus* **229**, 206–213.
- Kuebler K. E. (2013) A combined electron microprobe (EMP) and Raman spectroscopic study of the alteration products in Martian meteorite MIL 03346. *J. Geophys. Res. Planets* **118**, 347–368.
- Labidi J., Cartigny P. and Jackson M. G. (2015) Multiple sulfur isotope composition of oxidized Samoan melts and the implications of a sulfur isotope “mantle array” in chemical geodynamics. *Earth Planet. Sci. Lett.* **417**, 28–39.
- Lentz R. C. F., Taylor G. J. and Treiman A. H. (1999) Formation of a martian pyroxenite: a comparative study of the nakhlite meteorites and Theo’s Flow. *Meteorit. Planet. Sci.* **34**, 919–932.
- Macke R. J., Britt D. T. and Consolmagno G. J. (2011) Density, porosity, and magnetic susceptibility of achondritic meteorites. *Meteorit. Planet. Sci.* **46**, 311–326.
- Magna T., Day J. M. D., Mezger K., Fehr M. A., Dohmen R., Aoudjehane H. C. and Agee C. B. (2015) Lithium isotope constraints on crust-mantle interactions and surface processes on Mars. *Geochim. Cosmochim. Acta* **162**, 46–65.
- Mandeville C. W., Webster J. D., Tappen C., Taylor B. E., Timbal A., Sasaki A., Hauri E. and Bacon C. R. (2009) Stable isotope and petrologic evidence for open-system degassing during the climactic and pre-climactic eruptions of Mt. Mazama, Crater Lake. *Oregon. Geochim. Cosmochim. Acta* **73**, 2978–3012.
- McCanta M. C., Elkins-Tanton L. and Rutherford M. J. (2009) Expanding the application of the Eu-oxybarometer to the Lherzolithic shergottites and nakhlites: Implications for the oxidation state heterogeneity of the Martian interior. *Meteorit. Planet. Sci.* **44**, 725–745.
- McCubbin F. M., Elardo S. M., Shearer C. K., Smirnov A., Hauri E. H. and Draper D. S. (2013) A petrogenetic model for the comagmatic origin of chassignites and nakhlites: Inferences from chlorine-rich minerals, petrology, and geochemistry. *Meteorit. Planet. Sci.* **48**, 819–853.
- Mikouchi T., Koizumi E., Monkawa A., Ueda Y. and Miyamoto M. (2003) Mineralogy and petrology of Yamato 000593: comparison with other Martian nakhlite meteorites. *Antarct. Meteor. Res.* **16**, 34–57.
- Mikouchi T., Miyamoto M., Koizumi E., Makishima J. and McKay G., Relative burial depths of Nakhlites: an Update. In 37th Lunar and Planetary Science Conference (abstract #1865).
- O’Connell-Cooper C. D., Spray J. G., Thompson L. M., Gellert R., Berger J. A., Boyd N. I., Desouza E. D., Perrett G. M., Schmidt M. and VanBommel S. J. (2017) APXS-derived chemistry of the Bagnold dune sands: Comparisons with Gale crater soils and the global martian average. *J. Geophys. Res. Planets* **122**, 2623–2643.
- Richter F., Chaussidon M., Mendybaev R. and Kite E. (2016) Reassessing the cooling rate and geologic setting of Martian meteorites MIL 03346 and NWA 817. *Geochim. Cosmochim. Acta* **182**, 1–23.
- Righter K., Danielson L. R., Pando K., Morris R. V., Graff T. G., Agresti D. G., Martin A. M., Sutton S. R., Newville M. and Lanzirotti A. (2013) Redox systematics of martian magmas with implications for magnetite stability. *Am. Mineral.* **98**, 616–628.
- Righter K., Keller L. P., Rahman Z. and Christoffersen R. (2014) Redox-driven exsolution of iron-titanium oxides in magnetite in Miller Range (MIL) 03346 nakhlite: Evidence for post crystallization oxidation in the nakhlite cumulate pile? *Am. Mineral.* **99**, 2313–2319.
- Righter K., Yang H., Costin G. and Downs R. T. (2008) Oxygen fugacity in the Martian mantle controlled by carbon: New constraints from the nakhlite MIL 03346. *Meteorit. Planet. Sci.* **43**, 1709–1723.
- Rutherford M. J. and Hammer J. E. (2008) Oxidation states in MIL 03346 nakhlite from experiments reproducing phenocryst-melt equilibria as a function of  $fO_2$  and T at 40–150 MPa. In 39th Lunar and Planetary Science Conference (abstract #1983).
- Sautter V., Jambon A. and Boudouma O. (2006) Cl-amphibole in the nakhlite MIL 03346: Evidence for sediment contamination in a Martian meteorite. *Earth Planet. Sci. Lett.* **252**, 45–55.
- Szymanski A., Brenker F. E., Palme H. and El Goresy A. (2010) High oxidation state during formation of Martian nakhlites. *Meteorit. Planet. Sci.* **45**, 21–31.
- Treiman A. H. (2005) The nakhlite meteorites: Augite-rich igneous rocks from Mars. *Chem. Erde-Geochem.* **65**, 203–270.
- Treiman A. H. and Irving A. J. (2008) Petrology of Martian meteorite Northwest Africa 998 Available at: *Meteorit. Planet. Sci.* **43**, 829–854.
- Udry A., McSween H. Y., Lecumberri-Sanchez P. and Bodnar R. J. (2012) Paired nakhlites MIL 090030, 090032, 090136, and 03346: Insights into the Miller Range parent meteorite. *Meteorit. Planet. Sci.* **47**, 1575–1589.
- van der Plas L. and Tobi A. C. (1965) A chart for judging the reliability of point counting results. *Am. J. Sci.* **263**, 87–90.

Associate editor: Chris Herd